PAPER

MoS$_2$ nanoparticle/activated carbon composite as a dual-band material for absorbing microwaves†

Praveen Negi and Ashavani Kumar [ID] *

In the search for novel high-performance microwave (MW) absorbers, MoS$_2$ has shown promise as a MW-absorbing material, but its poor impedance matching limits its applications. Herein, a facile hydrothermal method was used to produce a composite consisting of activated carbon (AC) derived from waste biomass and *in situ*-grown MoS$_2$ nanoparticles. Its microwave absorption properties were examined in the 2–18 GHz frequency range, and FESEM and HRTEM images confirmed the formation of MoS$_2$ nanoparticles on the AC. The maximum reflection loss (RL$_{max}$) for the MoS$_2$/AC composite was −31.8 dB (@16.72 GHz) at 20 wt% filler loading. At 50 wt% filler loading, the MoS$_2$/AC (MAC50) composite exhibited unique dual-band absorption characteristics in the C and K$_u$ bands. An effective absorption bandwidth (RL < −10 dB) of 10.4 GHz (3–5.2 GHz, 9.8–18 GHz) was achieved at various thicknesses that covered the entire K$_u$ band. Therefore, a sole dielectric absorber can easily be tuned to absorb MWs at multiple frequency ranges. The large surface area and conduction losses of AC combined with the superior dielectric loss properties of MoS$_2$ resulted in improved impedance matching and attenuation ability of the MoS$_2$/AC composite. Thus, MoS$_2$/AC is a promising low-cost dielectric absorber for MW absorption applications.

1. Introduction

In the past decade, there has been a rapid surge in modern technology, especially in the fields of electronics and wireless communications. This has led to wide interest in developing novel microwave (MW)-absorbing materials. A high-performance MW absorber should strongly absorb with a wide effective absorption bandwidth (EAB), *i.e.*, the frequency range where reflection loss (RL) <−10 dB, and should also be lightweight, with good thermal stability, and the ability to tune MW absorption to desired frequency bands.[1,2]

A two-dimensional (2D) transition metal dichalcogenide, molybdenum disulphide (MoS$_2$), has shown promise as a microwave-absorbing material in recent years due to its large specific surface area and high dielectric properties.[1–4] Ning *et al.*[5] prepared 2D MoS$_2$ nanosheets using a top-down exfoliation method and reported a maximum reflection loss (RL$_{max}$) = −38.42 dB. Liang *et al.*[6] used a hydrothermal process to fabricate MoS$_2$ nanosheets and obtained an RL$_{max}$ value of −47.8 dB. To enhance the MW absorption properties of MoS$_2$, there are generally two approaches: first, to combine a magnetic material

with MoS$_2$ such as MoS$_2$/FeS$_2$,[7] MoS$_2$–iron oxide,[3] porous coin-like Fe@MoS$_2$,[8] or BaFe$_{12}$O$_{19}$@MoS$_2$,[9] and second, to incorporate a nonmagnetic or pure dielectric material with MoS$_2$.

A pure dielectric absorber faces the problem of poor impedance matching,[2] but in recently reported studies, it was demonstrated that when various carbon-based materials were combined with MoS$_2$, the MW absorption by a dielectric absorber was enhanced. An excellent EAB of 10.85 GHz was measured for the MoS$_2$-coated carbon fiber fabricated by Zhang *et al.*[10] The MoS$_2$/carbon nanotube (CNT) (2D/1D) composite synthesized by Sun *et al.* gave a maximum EAB = 5.60 GHz (RL$_{max}$ = −47.9 dB).[11] The MoS$_2$ nanosheet/3D carbon foam reported by Lyu *et al.*[12] yielded a RL$_{max}$ = −45.88 dB and EAB = 5.68 GHz, and the MoS$_2$/reduced graphene oxide (RGO) hybrid prepared by Wang *et al.* achieved a RL$_{max}$ = −50.9 dB and EAB of 5.72 GHz.[13] The EAB values of 5.92 GHz,[14] 6.96 GHz,[15] and 5.6 GHz (ref. 16) reported by other research groups confirm the enhanced MW absorption performance for the MoS$_2$/RGO composite.

Another carbon-based MoS$_2$ composite, *i.e.*, carbon spheres, has also been used to achieve superior MW-absorbing properties. The core–shell carbon-sphere CS/MoS$_2$ composite fabricated by Zhang *et al.*[4] provided a RL$_{max}$ = −52.6 dB (EAB = 6.29 GHz), whereas Ning *et al.*[2] encapsulated MoS$_2$ nanosheets in hollow carbon spheres and obtained an excellent RL$_{max}$ = −65 dB. The morphologically based study performed by Zhang *et al.*[17] also concluded that a MoS$_2$/carbon composite with a micro-sphere morphology provided a more optimal MW-absorbing

Department of Physics, National Institute of Technology Kurukshetra, Haryana 136119, India. E-mail: ashavani@yahoo.com; ashavani@nitkkr.ac.in

performance than pure MoS_2. The incorporation of carbon-based materials with MoS_2 provides multiple interfaces that increase interfacial polarization[14,17] and facilitate the multiple reflections of incident MWs.[3,4] It also improves impedance matching of the composite and thus reduces surface reflections.[2]

Recently, biomass-based activated carbon has emerged as a potential dielectric loss material for MW-absorbing applications.[18–23] The presence of natural and artificial porosity in the activated carbon facilitates multiple reflections and scattering of incident MWs.[21,22] Our group has also reported that mango leaf-based activated carbon is an excellent MW-absorbing material.[24] Therefore, due to its remarkable properties such as large surface area, adequate porosity, light weight, sustainable natural source, and low cost,[21,23] an activated carbon-based dielectric composite is a potential candidate for MW absorption applications.

In the present study, a MoS_2/activated carbon composite was synthesized, and its MW absorption properties were reported. The composite at 20 wt% filler loading yielded an RL_{max} = −31.8 dB at 16.72 GHz, whereas at 50 wt% filler loading, the absorber gave a dual-band RL in the C and K_u bands. The dual-band MW-absorption performances reported by Liu *et al.*[25] and Shu *et al.*[26] used co-doped NiZn ferrite/graphene and RGO/MWCNTs/$ZnFe_2O_4$ nanocomposites, respectively. These composites were constructed from dielectric and magnetic materials, whereas Zhang *et al.*[1] reported a solely dielectric-based VS_2 nanosheet that exhibited dual-band MW absorption in the C and K_u bands. Thus, the dual-band loss shown by the MoS_2/activated carbon (AC) composite is unique and, to the best of our knowledge, has not been reported for any MoS_2/carbon-based composites.

2. Experimental

2.1. Materials

Sodium molybdate dihydrate ($Na_2MoO_4 \cdot 2H_2O$) ACS grade and potassium hydroxide (KOH) AR grade were purchased from Merck Life Science Pvt. Ltd. L-Cysteine, paraffin wax, and hydrochloric acid (HCl) were purchased from Lobachemie Pvt. Ltd. Ethanol was purchased from Changshu Pvt. Ltd., and mango leaves were collected on the Institute premises.

2.2. Synthesis of the MoS_2/AC composite

Waste mango leaf-based AC was synthesized by a facile method of carbonization followed by its activation using KOH, as previously reported by our group.[24] The MoS_2/AC composite was prepared by a hydrothermal method. Sodium molybdate and L-cysteine (1 : 5 molar ratio) were dissolved in 30 ml of deionized (DI) water. After the AC in DI water was sonicated for 1 hour, both solutions were mixed and then stirred for 2 hours to form a uniform solution. The ratio of MoS_2 to AC was maintained at 1 : 0.5. The pH was decreased to approximately 2 by adding HCl to the solution. The 80 ml solution of sodium molybdate, L-cysteine, and AC was then transferred to a Teflon-lined stainless-steel autoclave (100 ml) and heated at 180 °C for 24 h. The as-prepared precipitate was then washed with DI water and ethanol using a centrifuge until a neutral pH was achieved. The washed sample was then dried in an oven at 100 °C overnight. The resulting MoS_2/AC composite was named MAC, and an illustration of the preparation of the MoS_2/AC composite is shown in Scheme 1.

2.3. Characterization

Powder X-ray diffraction (XRD) was performed using a Rigaku Miniflex II with Cu Kα radiation (λ = 1.54 Å). A confocal micro-Raman spectrometer (AIRIX CORP) with laser excitation at 532 nm was used to obtain Raman spectra. The morphology was studied by field emission scanning electron microscopy (FESEM, FEI Nova Nano) and high-resolution transmission electron microscopy (HRTEM, FEI Tecnai G2 20 S-TWIN). A Thermo Fisher Scientific Nexsa base was used to record X-ray photoelectron spectra (XPS). A Quantachrome Nova 2200e was used to measure nitrogen adsorption–desorption isotherms at 77.3 K. A multiple points Brunauer–Emmett–Teller (BET) method was used to calculate the specific surface area, and the Barrett, Joyner, and Halenda (BJH) model was used to calculate the pore size distribution.

2.4. Microwave absorption measurements

To study the microwave absorption properties, MAC powder and paraffin wax were mixed and heated at 100 °C. The mixture was then pressed into a toroidal shape (φ_{out} = 7.0 mm, φ_{in} = 3.0 mm) using a die. The wt% of MAC in wax was varied, and 10%, 20%, 30%, 40%, and 50% were tested. Therefore, the samples were named MAC10, MAC20, MAC30, MAC40, and MAC50, where the numbers represent the loading wt% of MAC in paraffin wax.

An Agilent E8364B PNA series vector network analyzer (VNA) was used to obtain the relative complex permittivity (ε_r) and permeability (μ_r) in the frequency range of 2–18 GHz. The RL values were calculated by the following eqn (1) and (2):[2,14]

$$RL\ (dB) = 20 \log|(Z_{in} - Z_0)/(Z_{in} + Z_0)| \tag{1}$$

$$Z_{in} = Z_0 \sqrt{\mu_r/\varepsilon_r}\tanh\left[j\frac{2\pi fd}{c}\sqrt{(\mu_r\varepsilon_r)}\right] \tag{2}$$

where Z_{in} denotes the input impedance of the absorber, Z_0 denotes the impedance of free space, c denotes the velocity of electromagnetic waves in free space, d denotes the thickness of the absorber, and f denotes the frequency of the electromagnetic waves.

3. Results and discussion

3.1. Morphological and structural analyses

Fig. 1a depicts the XRD pattern of AC where the broad peak at 2θ = 23.6° corresponds to the (002) plane and a weak peak at 2θ = 43.2° corresponds to the (100) plane. These two planes confirm the graphitic nature of AC.[18,24,27] These broad and weak peaks of AC indicate the low level of crystallinity and amorphous nature of porous AC.[18] The XRD pattern of the MoS_2/AC composite as shown in Fig. 1b contains characteristic diffraction peaks at 2θ
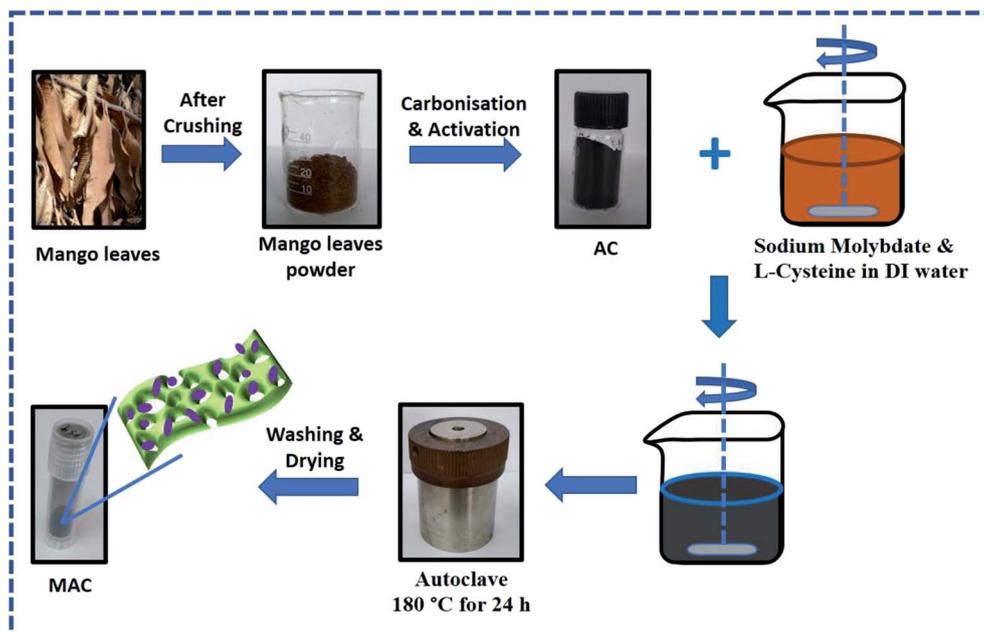
Scheme 1 Schematic illustration for the preparation of the MoS_2/AC composite.
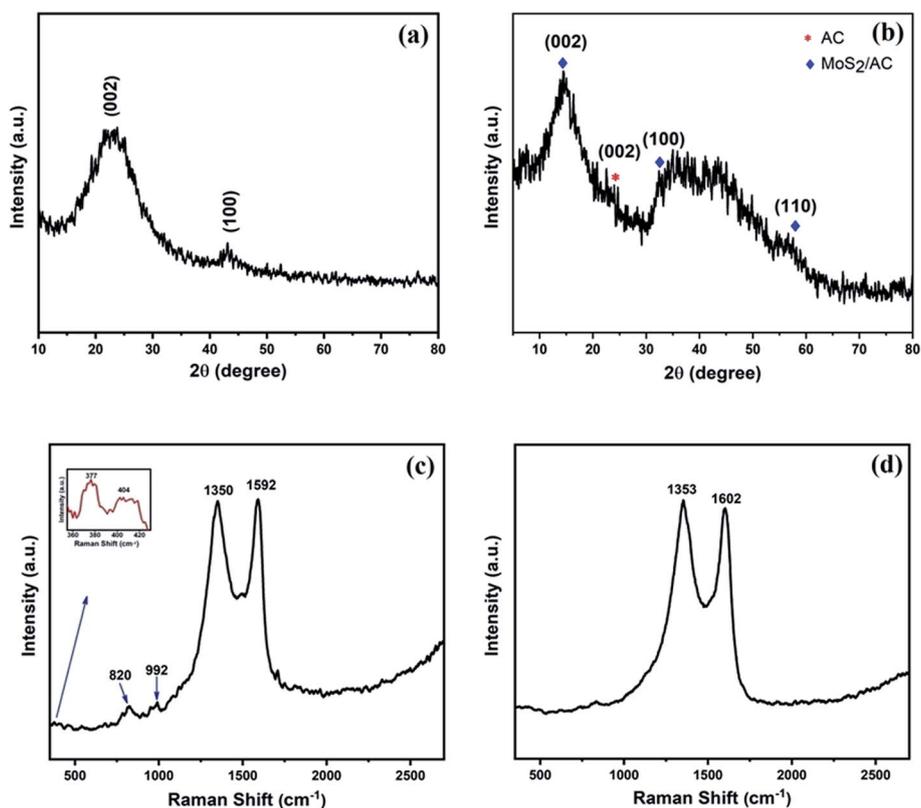

Fig. 1 XRD pattern of (a) activated carbon (AC) and (b) MoS_2/AC composite (MAC), and Raman spectrum of (c) MAC and (d) AC.

$= 14.3°$, $32.6°$, and $58.2°$ that correspond to the (002), (100), and (110) planes of MoS_2, respectively (JCPDS card no. 37-1492).[2,4,15] The broadening of peaks implies the formation of nano-sized MoS_2 particles[28] that were further confirmed by FESEM and HRTEM images. The intensity of the (002) plane of AC in the MoS_2/AC composite was suppressed, and this can be attributed to the formation of MoS_2 nanoparticles on the surface of carbon sheets as well as the low crystallinity of AC.[13]
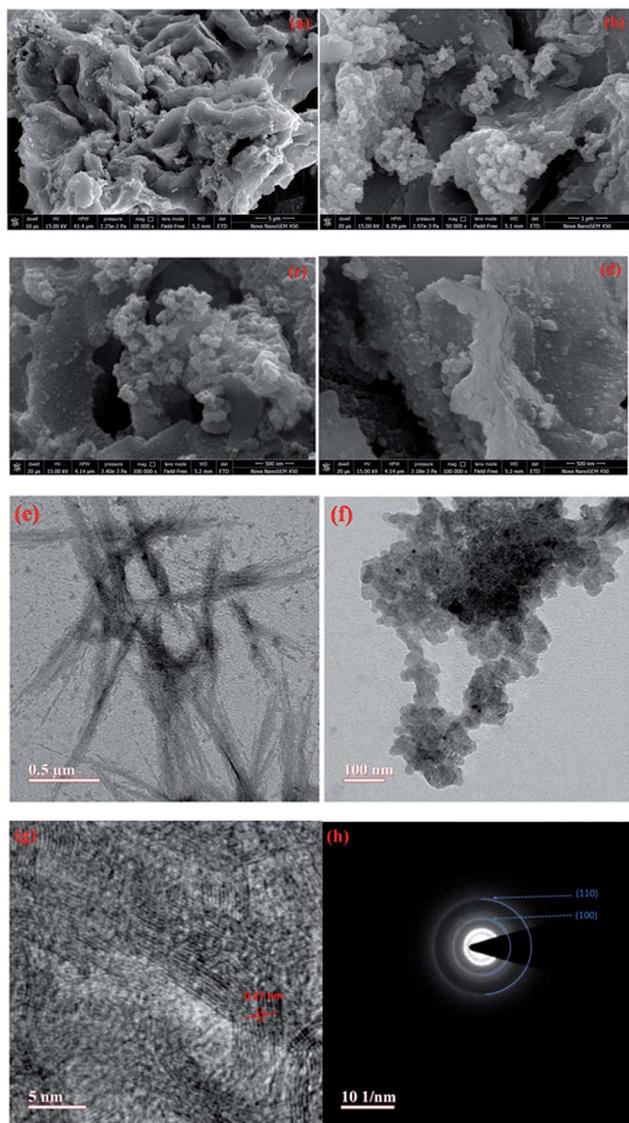
Fig. 2 (a–d) FESEM images, (e, f) TEM images, (g) HRTEM image, and (h) SAED pattern of MAC.

The nitrogen adsorption–desorption isotherm as depicted in Fig. S1† was obtained to study the porosity of AC. The activation process by KOH resulted in a large specific surface area (S_{BET} = 995.129 m^2 g^{-1}). The BJH pore size distribution (Fig. S1† inset) revealed that the total pore volume was 0.513 cm^3 g^{-1}, and the majority of pore sizes were in the range of 2–26 nm, which indicates the presence of mesopores in the AC.[29] The presence of AC in the MoS_2/AC composite was further confirmed by Raman analysis, as shown in Fig. 1c. The two strong peaks present at 1350 cm^{-1} (D band) and 1592 cm^{-1} (G band) are characteristic of graphitic carbon.[3,24] The G band arose due to the E_{2g} vibrational mode present within the aromatic carbon rings,[30] and it also represents the degree of graphitization.[31] The D band is attributed to the defects and disorder introduced into sp^2 carbon.[27,31,32]

When compared with the Raman spectra of AC (Fig. 1d), which exhibited a D band at 1353 cm^{-1} and G band at

1602 cm^{-1}, a blueshift was observed for the MAC Raman spectra, which can be attributed to the stress induced in AC by the formation of MoS_2 nanoparticles.[33] The two weak peaks at 377 cm^{-1} and 404 cm^{-1} shown in the Fig. 1c inset are the first-order Raman modes present in MoS_2, and these modes are associated with in-plane vibration (E_{2g}^1) and out-of-plane vibration (A_{1g}), respectively.[2,13,34] The other minor peaks at approximately 820 cm^{-1} and 992 cm^{-1} are attributed to the partial oxidation of MoS_2 (ref. 34 and 35) by the laser power used in Raman spectroscopy.[36]

The FESEM images shown in Fig. 2(a–d) depict the distribution of MoS_2 particles over the AC. The voids and pores formed in the carbon structure due to the activation process serve as a nucleation site for MoS_2 nanoparticles, hence the nanoparticles are also visible inside the pores (Fig. 2(c and d)). The majority of nanoparticles are in the range of 60 to 80 nm, as depicted in the particle size distribution graph of MoS_2 nanoparticles (Fig. S2†). The TEM images clearly depict the AC sheets (Fig. 2e), as well as the formation of the nano-sized MoS_2 particles (Fig. 2f). The HRTEM image depicted in Fig. 2g shows interlayer spacing of 0.27 nm that corresponds to the (100) plane of MoS_2,[37,38] whereas the selected area electron diffraction (SAED) pattern given in Fig. 2h resulted from the (100) and (110) planes of MoS_2.[13,16]

X-ray photoelectron spectroscopy (XPS) was performed to analyze the chemical composition and oxidation states of the elements present in the MoS_2/AC composite. Fig. 3a shows the full XPS spectrum of the composite, which confirms the presence of Mo, S, C, and O elements.[14,39,40] The atomic percents of Mo, S, and C were 12.64%, 26.73%, and 22.16%, respectively. The atomic ratio of Mo and S is 1 : 2.1, which is very close to the theoretical value of MoS_2, whereas the atomic ratio of MoS_2 and carbon is approximately 1 : 0.56, which is quite close to the initial precursor values. Fig. 3b depicts the high-resolution spectrum of Mo 3d, in which the Mo $3d_{5/2}$ and Mo $3d_{3/2}$ orbitals at approximately 229.5 eV and 232.7 eV, respectively, determine the existence of Mo^{4+}.[2,3,15] Fig. 3c shows the high-resolution spectra of C 1s, which was de-convoluted into three peaks. The most dominating peak at approximately 285 eV corresponds to the C–C/C=C group, while the minor peaks at approximately 286.5 eV and 288.3 eV correspond to the C–O and C=O groups, respectively.[2,3,15] The S 2p high-resolution spectrum depicted in Fig. 3d was de-convoluted into three peaks. The peaks at approximately 162.5 eV and 163.7 eV correspond to the $2p_{3/2}$ and $2p_{1/2}$ orbitals[40,41] respectively, whereas the peak at approximately 164.9 eV corresponds to the C–S–C group.[39,42,43]

3.2. Microwave absorption properties

To study the microwave absorption properties of an absorber, the two important parameters, i.e., ε_r and μ_r were obtained from VNA. Because both MoS_2 and AC are nonmagnetic materials, hence the value of μ_r was taken to be 1. The ε_r consists of two parts: the real part of permittivity (ε') represents the storage of energy, whereas the imaginary part of permittivity (ε'') represents the energy dissipation.[4]
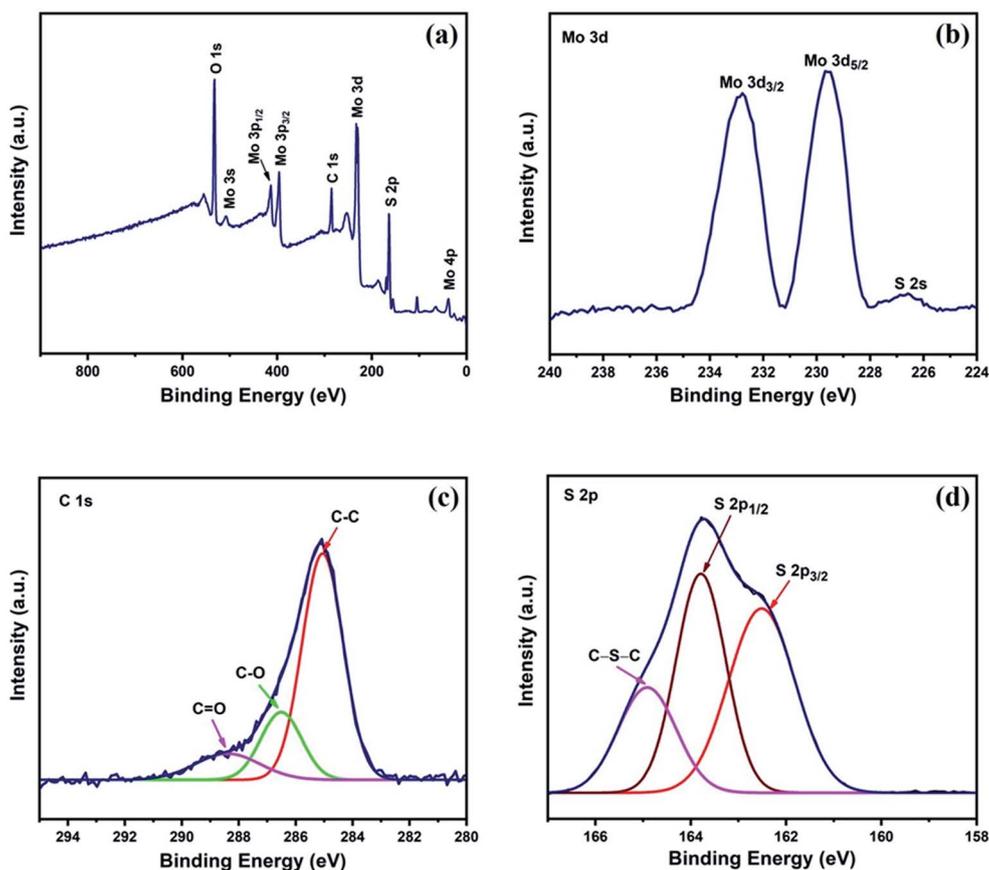
Fig. 3 (a) XPS survey spectra and high resolution spectra of (b) Mo 3d, (c) C 1s, and (d) S 2p for MAC.

The value of ε' for all the samples shows a decreasing trend with increase in frequency, with minor fluctuations as shown in Fig. 4a. The ε' value for MAC10, MAC20, MAC30, MAC40, and MAC50 are in the range of 2.69–2.57, 3.95–3.49, 5.19–4.54, 7.58–6.33, and 11.68–9.08, respectively. The value of ε' increases with increasing concentration of MAC in paraffin wax, as per effective medium theory,[2,4,15] and the increase in MAC in paraffin wax leads to an increase in interfacial polarization. Multiple interfaces within the paraffin matrix are created by the porous structure of AC along with the MoS_2 nanoparticles, which amplifies the interfacial polarization. Hence, there will be clear increases in the values of ε' with increasing filler (MAC) loading.
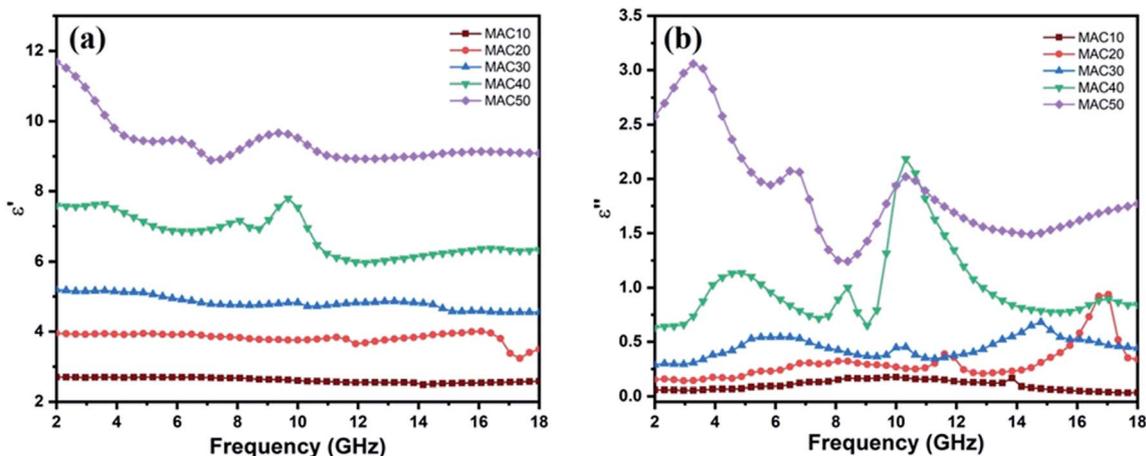

Fig. 4 (a) The real part and (b) imaginary part of the relative complex permittivity of the MAC–paraffin wax composite with different filler loadings ranging from 10 wt% to 50 wt%.
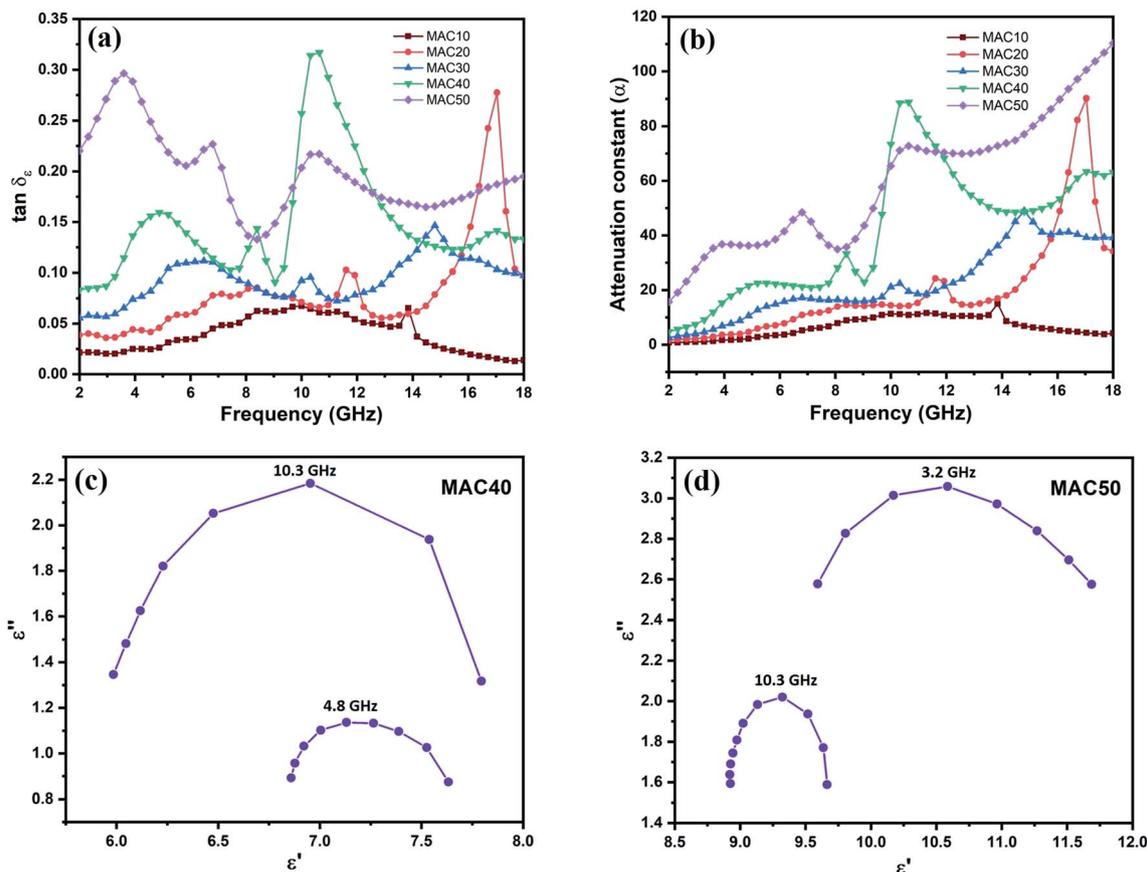
Fig. 5 (a) Dielectric loss tangent and (b) attenuation constant (α) of MAC−paraffin wax composites with different filler loadings ranging from 10 wt% to 50 wt%; Cole−Cole plot of (c) MAC40 and (d) MAC50.

Similar to ε', the ε'' values as depicted in Fig. 4b also show an increasing trend with increasing filler (MAC) loading. This can be attributed to the increase in the AC content, which increases the electrical conductivity of sample. According to free electron theory: $\varepsilon'' \approx 1/(2\pi\varepsilon_0 f\rho)^{-1}$,[3,44] where ρ denotes the resistivity of an absorber, ε_0 denotes the permittivity of free space, and f denotes the electromagnetic (EM) wave frequency. Therefore, increasing the carbon content decreases the electrical resistivity of the absorber, which increases the ε'' value. As the MAC loading increased above 10 wt%, several relaxation peaks were obtained in the complex permittivity.[5] Fig. S3(a–d)† shows two peaks for MAC20 and MAC30, whereas there are 3 peaks for MAC40 and MAC50. The peak in the frequency range of 10–12 GHz is common in all the graphs, which suggests that the complex permittivity of the MAC–wax composite has a resonant characteristic,[45,46] and this resonance peak can be attributed to relaxation from the MoS$_2$–AC interfaces.[47] Because the dipoles were created by asymmetrical charge distribution in the AC due to the presence of pores and defects, dipole orientation polarization results.[46,48,49] When these dipoles cannot maintain the pace of the changing EM field, polarization relaxation occurs.[50] These polarization relaxations are responsible for the other relaxation peaks shown at 17 GHz in Fig. S3a,† 14.8 GHz in Fig. S3b,† 4.8 and 8.4 GHz in Fig. S3c,† and 3.2 and 6.8 GHz in Fig. S3d.†

To understand the mechanism of MW absorption inside the absorber, the dielectric loss tangent[17] (Fig. 5a) and the attenuation constant (α)[1,2] (Fig. 5b) were calculated using eqn (3) and (4), respectively.

$$\tan \quad \delta_\varepsilon = \varepsilon''/\varepsilon' \tag{3}$$

$$\alpha = \frac{\sqrt{2}\pi f}{c} \times \sqrt{(\mu''\varepsilon'' - \mu'\varepsilon') + \sqrt{(\mu''\varepsilon'' - \mu'\varepsilon')^2 + (\mu'\varepsilon'' - \mu''\varepsilon')^2}} \tag{4}$$

where c denotes the speed of light and f denotes the frequency. The dielectric loss value as well as the attenuation constant of the MAC composite increase with the increase in filler loading with many relaxation peaks. It is clear from Fig. 5a that MAC50 has the tan δ_ε maximum value, except in the frequency range of 9.7–12.4 GHz and 16.3–17.3 GHz, where MAC40 and MAC20 dominate, respectively. This occurred because of the resonance peak of relative permittivity for MAC20 and MAC40, which enhanced their dielectric loss in these specific frequency range. A similar trend was observed for α values, in which the highest value was obtained for MAC50 except in the frequency range 9.8–11.6 GHz.

Dielectric relaxation plays an important role in the MW absorption performance of an absorber. Based on the Debye dipolar relaxation,[14,51] the relationship between ε' and ε'' can be written as:
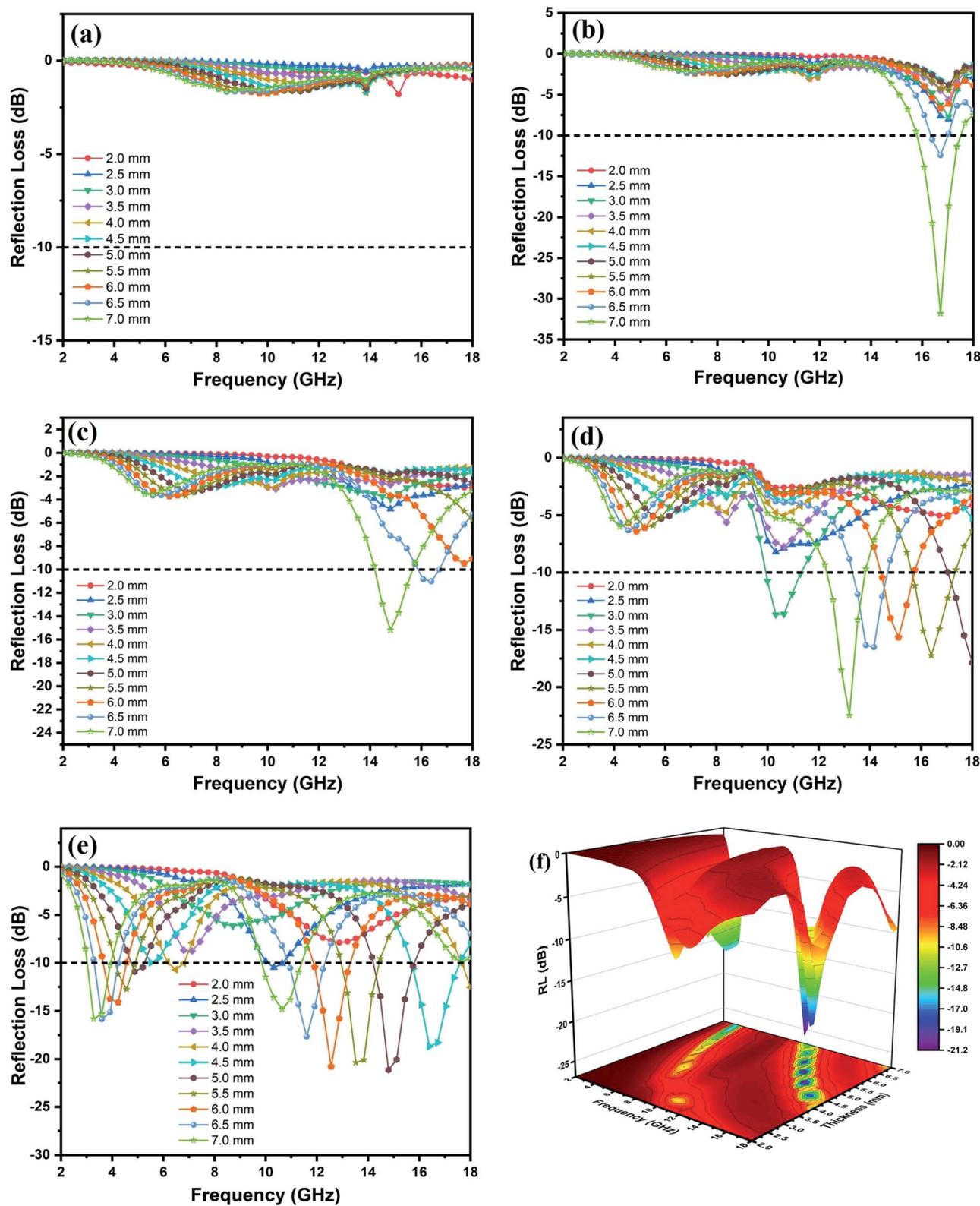
Fig. 6   Reflection loss curves of (a) MAC10, (b) MAC20, (c) MAC30 (d) MAC40, (e) MAC50, and (f) 3-D graph of MAC50 at thicknesses ranging from 2 mm to 7 mm.
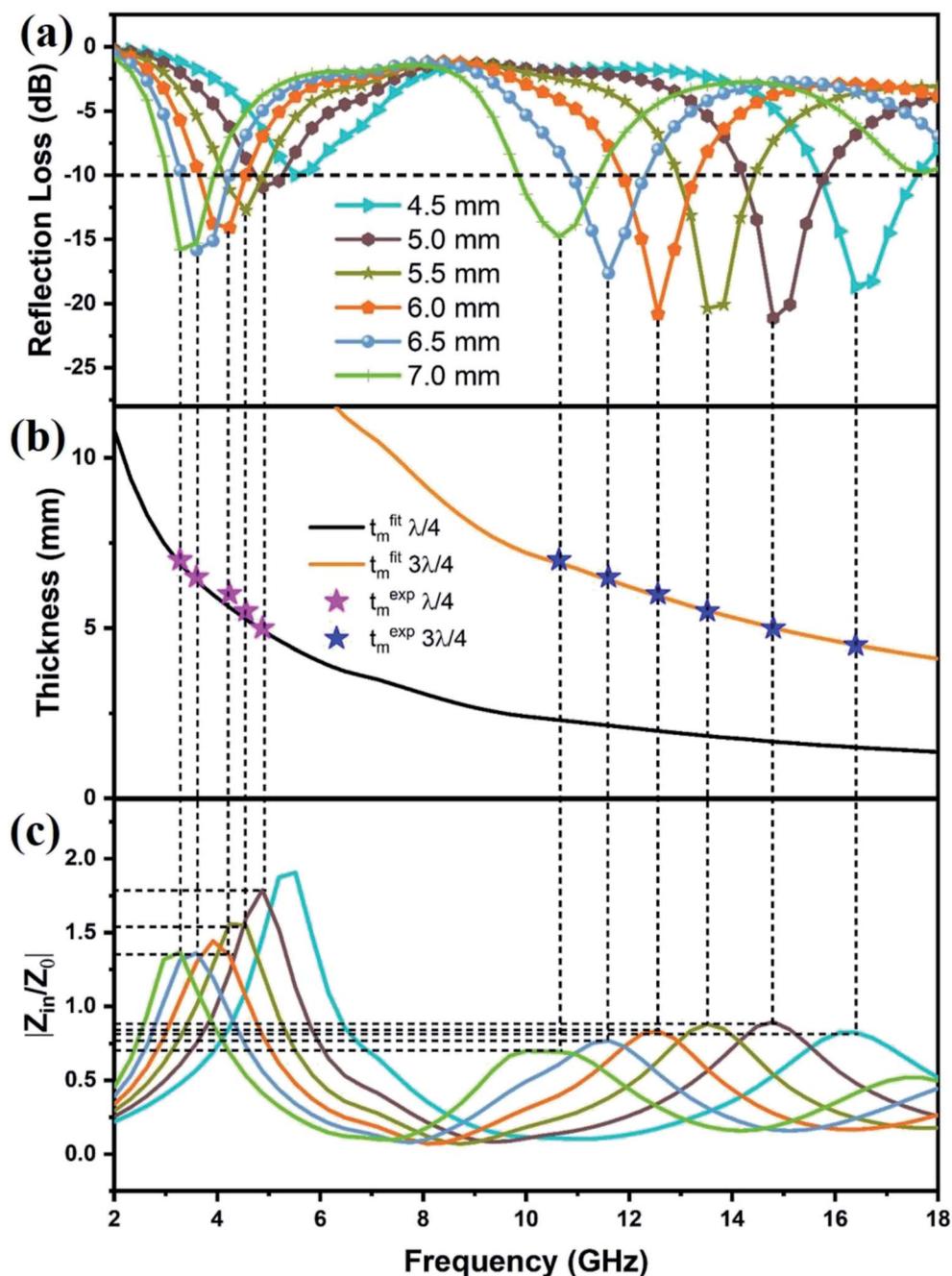
Fig. 7 (a) The RL-frequency curves of MAC50 with absorber thickness from 4.5 mm to 7 mm; (b) relationship between t_m^{fit}, t_m^{exp}, and the peak frequency of MAC50 under the $n\lambda/4$ model, and (c) the relationship between $|Z_{in}/Z_0|$ and frequency for MAC50.

$$\left(\varepsilon' - \frac{\varepsilon_s + \varepsilon_\infty}{2}\right)^2 + (\varepsilon'')^2 = \left(\frac{\varepsilon_s + \varepsilon_\infty}{2}\right)^2 \quad (5)$$

where ε_s and ε_∞ represent the static dielectric constant and the dielectric constant at infinite frequency, respectively. Eqn (5) can be used to explain the semicircle curve formed between ε' and ε'' and these semicircles are denoted as Cole–Cole semicircles. Each semicircle corresponds to one Debye relaxation process.[3,51] Fig. 5(c, d) shows that MAC40 and MAC50 contain two large semicircles. The semicircle present at approximately 10.3 GHz in both MAC40 and MAC50 can be attributed to the

dielectric relaxation process due to the MoS$_2$–AC interfacial polarization.[47] The other semicircles at 4.8 GHz (Fig. 5c) and 3.2 GHz (Fig. 5d) suggest additional dielectric relaxation, which can be due to pores and defects present in the MAC composite.[48,49,52] At lower filler loadings (MAC10, MAC20, and MAC30), as depicted in Fig. S4(a–c),† distorted curves instead of semicircles appear, which suggest poor dielectric loss capabilities of these samples.

Impedance matching is another important characteristic of an absorber for enhanced MW-absorbing properties. It is

represented by the relation $Z = |Z_{in}/Z_0|$, where Z_0 denotes the impedance of air.[2,23] The closer the value of Z to 1, the greater the amount of microwaves that can enter the absorber and thus reduce the direct reflections of MWs from the surface of an absorber. Fig. S5(a–e)† shows a curve of impedance matching with frequency. The peak values of Z range between 11.43 to 34.63 for MAC10, 7.34 to 11.86 for MAC20, 5.1 to 7.7 for MAC30, 2.68 to 4.52 for MAC40, and 1.36 to 3 for MAC50. It is clear from the Z values that as the filler loading of MAC increases, the absorber exhibits more optimal impedance-matching characteristics.

Fig. 6(a–e) depicts the RL curve for five different loadings of MAC at thicknesses ranging from 2 to 7 mm. At 10 wt% MAC loading (Fig. 6a), the sample did not show any significant RL values, and the low amount of filler loading resulted in low dielectric losses that led to poor MW absorption by MAC10. As the filler loading increased to 20 wt% (MAC20, Fig. 6b), the highest RL value of −31.8 dB at 16.72 GHz (7 mm) was obtained. This enhanced MW-absorbing performance can be attributed to the higher values of α and $\tan \delta_\varepsilon$ along with more optimal impedance matching (Fig. S6†) in the frequency range of 16–17 GHz. Fig. 6c shows the RL curve for MAC30, and due to low attenuation constant values, RL values above −10 dB were only achieved at thicknesses of 6.5 and 7 mm (RL$_{max}$ = −14.8 GHz, EAB = 1.47 GHz).

As the filler loading reached 40 wt% in sample MAC40 (Fig. 6d), the RL$_{max}$ value of −22.47 dB at 7 mm thickness was achieved, and the RL values below −10 dB for thicknesses of 5–7 mm covered the frequency range from 12.2 to 18 GHz, which included almost the entire K$_u$ band. An EAB of 1.37 GHz at a thickness of only 3 mm was also obtained for the sample. As the filler loading increased from 10 to 40 wt%, one can clearly see an improvement in the RL values in the lower frequency range (4 to 6 GHz), as the RL value reached 5 dB for thicknesses above 5 mm.

Fig. 6e and f show the 2D and 3D RL graph for MAC50, respectively. It clearly depicts the further improvement in the RL values in the frequency range of 3–5.2 GHz, reaching to −15.86 dB for 6.5 mm thickness. Thus, the RL values above −10 dB were achieved in two different frequency bands, i.e., the C and K$_u$ bands, which resulted in dual-band MW absorption characteristics. The RL$_{max}$ = −21.13 dB was obtained at 14.8 GHz for 5 mm thickness, whereas the maximum EAB of 2.45 GHz was obtained at 7 mm thickness. Therefore, MAC50 contributed the most optimal MW-absorbing performance out of all the samples. The RL <−10 dB covered approximately 10.4 GHz (3–5.2 GHz, 9.8–18 GHz) for various thicknesses.

From Fig. 7a, it is clear that the maximum value of RL gradually shifts towards a lower frequency with the increasing thickness of the absorber. The thickness of an absorber plays an important role in the MW-absorbing performance. This behavior can be explained by the quarter wavelength matching model:[26,53]

$$t_m = \frac{n\lambda}{4} \frac{nc}{4fm\sqrt{|\varepsilon_r||\mu_r|}} \quad (n = 1, \ 3, \ 5\ldots) \tag{6}$$
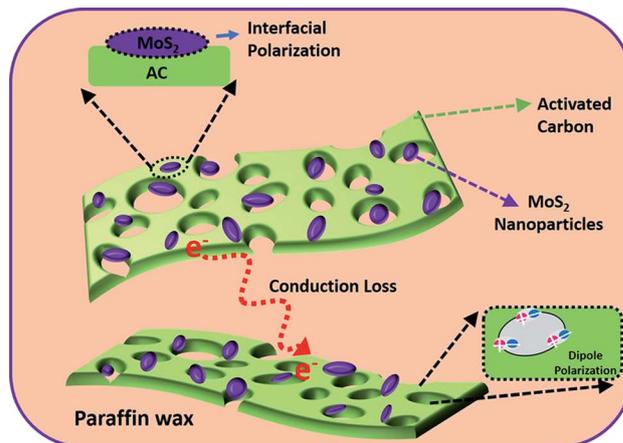
Scheme 2 Schematic illustration of the MW absorption mechanism in the MAC–paraffin wax composite.

where f_m, t_m, and c denote the matching frequency, matching thickness, and speed of light, respectively. The satisfaction of eqn (6) at a particular thickness and frequency results in a phase difference of π between the reflected microwave of the air–absorber and absorber–metal interfaces. This leads to the cancellation of both the microwaves at the air–absorber interface.[54] Fig. 7b and S7b† depict the relationship between t_m^{fit} (thickness calculated by using eqn (6)) and t_m^{exp} (experimental thickness) for MAC50 and MAC40, respectively. The pink colour stars lie on the $\lambda/4$ curve, and the blue colour stars lie on the $3\lambda/4$ curve. This agreement between t_m^{fit} and t_m^{exp} suggests that both samples obey the $n\lambda/4$ model. Therefore, the quarter wavelength matching theory is a valuable tool for achieving the optimum MW-absorbing performance for an absorber by tuning its thickness according to the desired frequency.

Fig. 7a, c, S7(a, c), and S6† show the relationships between reflection loss and impedance matching for MAC50, MAC40, and MAC20, respectively. It is evident from the graphs that the closer the values of Z to 1, the more optimal the RL values. At 7 mm thickness for MAC20, the value of Z reaches approximately 1, hence, the RL reaches a maximum of −31.8 dB.

The mechanism for enhanced MW absorption performance in MAC50 can be explained as depicted in Scheme 2. First, the increase in conductivity due to the incorporation of AC resulted in the migration of additional electrons, and those then convert the EM energy by colliding with the lattice,[55] leading to high conduction losses.[19,23,56] It also improved the impedance matching and reduced the surface reflection of MWs, allowing more MWs to enter the absorber. Second, the combination of AC and MoS$_2$ in the paraffin wax resulted in multiple interfaces, thus increasing the interfacial polarization. Third, the asymmetrical charge distribution due to the pores and defects present in the AC resulted in the formation of dipoles.[46] These dipoles under an alternating EM field rotate to align themselves with the EM field and thus convert the EM energy into heat.[55] Therefore, it is concluded that MoS$_2$/AC has the potential for MW absorption applications.

4. Conclusions

A MoS_2/AC composite was successfully synthesized by a hydrothermal method. The incorporation of biomass (mango leaves)-based AC played a key role in improving the MW absorption performance of the MAC composite. The maximum RL value of −31.8 dB was achieved with a filler loading of only 20 wt%. It was also found that a filler loading of 50 wt% MAC in paraffin wax resulted in a unique dual-band absorption property in C and K_u bands. Impressively, an EAB of 10.4 GHz (3–5.2 GHz, 9.8–18 GHz) was achieved at thicknesses ranging from 4.5 mm to 7 mm. The synergistic effects between the MoS_2 nanoparticles and AC resulted in high impedance matching, multiple reflections, and improved attenuation constant values, which contributed to the enhancement of the MW absorption properties of MoS_2/AC. These results suggest that MoS_2/AC is a promising dielectric dual-band MW absorber for practical applications. This study can also be extended to other combinations of biomass-based carbon with MoS_2 for designing novel MW absorbers.

Conflicts of interest

There are no conflicts to declare.

Acknowledgements

References

1 D. Zhang, H. Zhang, J. Cheng, H. Raza, T. Liu, B. Liu, X. Ba, G. Zheng, G. Chen and M. Cao, *J. Mater. Chem. C*, 2020, **8**, 5923–5933.

2 M. Ning, Q. Man, G. Tan, Z. Lei, J. B. Li and R. W. Li, *ACS Appl. Mater. Interfaces*, 2020, **12**, 20785–20796.

3 D. Zhang, J. Chai, J. Cheng, Y. Jia, X. Yang, H. Wang, Z. Zhao, C. Han, G. Shan, W. Zhang, G. Zheng and M. Cao, *Appl. Surf. Sci.*, 2018, **462**, 872–882.

4 F. Zhang, W. Zhang, W. Zhu, B. Cheng, H. Qiu and S. Qi, *Appl. Surf. Sci.*, 2019, **463**, 182–189.

5 M. Q. Ning, M. M. Lu, J. B. Li, Z. Chen, Y. K. Dou, C. Z. Wang, F. Rehman, M. S. Cao and H. B. Jin, *Nanoscale*, 2015, **7**, 15734–15740.

6 X. Liang, X. Zhang, W. Liu, D. Tang, B. Zhang and G. Ji, *J. Mater. Chem. C*, 2016, **4**, 6816–6821.

7 L. Xing, X. Li, Z. Wu, X. Yu, J. Liu, L. Wang, C. Cai, W. You, G. Chen, J. Ding and R. Che, *Chem. Eng. J.*, 2020, **379**, 122241.

8 J. Pan, X. Sun, T. Wang, Z. Zhu, Y. He, W. Xia and J. He, *Appl. Surf. Sci.*, 2018, **457**, 271–279.

9 M. Wang, Y. Lin, H. Yang, Y. Qiu and S. Wang, *J. Alloys Compd.*, 2020, **817**, 153265.

10 W. Zhang, X. Zhang, Q. Zhu, Y. Zheng, L. F. Liotta and H. Wu, *J. Colloid Interface Sci.*, 2021, **586**, 457–468.

11 Y. Sun, W. Zhong, Y. Wang, X. Xu, T. Wang, L. Wu and Y. Du, *ACS Appl. Mater. Interfaces*, 2017, **9**, 34243–34255.

12 L. Lyu, F. Wang, B. Li, X. Zhang, J. Qiao, Y. Yang and J. Liu, *J. Colloid Interface Sci.*, 2021, **586**, 613–620.

13 Y. Wang, D. Chen, X. Yin, P. Xu, F. Wu and M. He, *ACS Appl. Mater. Interfaces*, 2015, **7**, 26226–26234.

14 X. Ding, Y. Huang, S. Li, N. Zhang and J. Wang, *Composites, Part A*, 2016, **90**, 424–432.

15 M. Ning, B. Kuang, Z. Hou, L. Wang, J. Li, Y. Zhao and H. Jin, *Appl. Surf. Sci.*, 2019, **470**, 899–907.

16 D. Zhang, Y. Jia, J. Cheng, S. Chen, J. Chai, X. Yang, Z. Wu, H. Wang, W. Zhang, Z. Zhao, C. Han, M. Cao and G. P. Zheng, *J. Alloys Compd.*, 2018, **758**, 62–71.

17 W. Zhang, X. Zhang, H. Wu, H. Yan and S. Qi, *J. Alloys Compd.*, 2018, **751**, 34–42.

18 X. Qiu, L. Wang, H. Zhu, Y. Guan and Q. Zhang, *Nanoscale*, 2017, **9**, 7408–7418.

19 Z. Wu, K. Tian, T. Huang, W. Hu, F. Xie, J. Wang, M. Su and L. Li, *ACS Appl. Mater. Interfaces*, 2018, **10**, 11108–11115.

20 L. Wang, P. Zhou, Y. Guo, J. Zhang, X. Qiu, Y. Guan, M. Yu, H. Zhu and Q. Zhang, *RSC Adv.*, 2019, **9**, 9718–9728.

21 H. Zhao, Y. Cheng, H. Lv, G. Ji and Y. Du, *Carbon*, 2019, **142**, 245–253.

22 H. Guan, H. Wang, Y. Zhang, C. Dong, G. Chen, Y. Wang and J. Xie, *Appl. Surf. Sci.*, 2018, **447**, 261–268.

23 L. Liu, S. Yang, H. Hu, T. Zhang, Y. Yuan, Y. Li and X. He, *ACS Sustainable Chem. Eng.*, 2019, **7**, 1228–1238.

24 P. Negi, A. K. Chhantyal, A. K. Dixit, S. Kumar and A. Kumar, *Sustainable Mater. Technol.*, 2021, **27**, e00244.

25 P. Liu, Z. Yao, J. Zhou, Z. Yang and L. B. Kong, *J. Mater. Chem. C*, 2016, **4**, 9738–9749.

26 R. Shu, W. Li, X. Zhou, D. Tian, G. Zhang, Y. Gan, J. Shi and J. He, *J. Alloys Compd.*, 2018, **743**, 163–174.

27 W. Gu, J. Sheng, Q. Huang, G. Wang, J. Chen and G. Ji, *Nano-Micro Lett.*, 2021, **13**, 102.

28 H. Liu, X. Chen, L. Deng, M. Ding, J. Li and X. He, *J. Mater. Chem. A*, 2016, **4**, 17764–17772.

29 K. S. W. Sing, D. H. Everett, R. A. W. Haul, L. Moscou, R. A. Pierotti, J. Rouquerol and T. Siemieniewska, *Pure Appl. Chem.*, 1985, **57**, 603–619.

30 L. Sun, C. Tian, M. Li, X. Meng, L. Wang, R. Wang, J. Yin and H. Fu, *J. Mater. Chem. A*, 2013, **1**, 6462–6470.

31 V. C. Tung, M. J. Allen, Y. Yang and R. B. Kaner, *Nat. Nanotechnol.*, 2009, **4**, 25–29.

32 H. Zhou, J. Zhang, I. S. Amiinu, C. Zhang, X. Liu, W. Tu, M. Pan and S. Mu, *Phys. Chem. Chem. Phys.*, 2016, **18**, 10392–10399.

33 G. Katumba, B. W. Mwakikunga and T. R. Mothibinyane, *Nanoscale Res. Lett.*, 2008, **3**, 421–426.

34 S. Mignuzzi, A. J. Pollard, N. Bonini, B. Brennan, I. S. Gilmore, M. A. Pimenta, D. Richards and D. Roy, *Phys. Rev. B*, 2015, **91**, 195411.

35 G. Mestl, P. Ruiz, B. Delmon and H. Knözinger, *J. Phys. Chem.*, 1994, **98**, 11269–11275.

36 B. C. Windom, W. G. Sawyer and D. W. Hahn, *Tribol. Lett.*, 2011, **42**, 301–310.

37 C. P. Veeramalai, F. Li, Y. Liu, Z. Xu, T. Guo and T. W. Kim, *Appl. Surf. Sci.*, 2016, **389**, 1017–1022.

38 S. V. P. Vattikuti, P. C. Nagajyothi, P. Anil Kumar Reddy, M. Kotesh Kumar, J. Shim and C. Byon, *Mater. Res. Lett.*, 2018, **6**, 432–441.

39 H. Liu, H. Hu, J. Wang, P. Niehoff, X. He, E. Paillard, D. Eder, M. Winter and J. Li, *ChemElectroChem*, 2016, **3**, 922–932.

40 Q. Tian, W. Wu, S. Yang, J. Liu, W. Yao, F. Ren and C. Jiang, *Nanoscale Res. Lett.*, 2017, **12**, 221.

41 J. Wang, X. Lin, Z. Chu, Z. Huang, T. Guo, L. Yang and S. Li, *Nanotechnology*, 2020, **31**, 135602.

42 L. L. Feng, G. D. Li, Y. Liu, Y. Wu, H. Chen, Y. Wang, Y. C. Zou, D. Wang and X. Zou, *ACS Appl. Mater. Interfaces*, 2015, **7**, 980–988.

43 T. Wu, M. Jing, L. Yang, G. Zou, H. Hou, Y. Zhang, Y. Zhang, X. Cao and X. Ji, *Adv. Energy Mater.*, 2019, **9**, 1803478.

44 M. S. Cao, W. L. Song, Z. L. Hou, B. Wen and J. Yuan, *Carbon*, 2010, **48**, 788–796.

45 X. L. Shi, M. S. Cao, J. Yuan, Q. L. Zhao, Y. Q. Kang, X. Y. Fang and Y. J. Chen, *Appl. Phys. Lett.*, 2008, **93**, 183118.

46 X. X. Wang, W. Q. Cao, M. S. Cao and J. Yuan, *Adv. Mater.*, 2020, **32**, 2002112.

47 L. Yan, J. Liu, S. Zhao, B. Zhang, Z. Gao, H. Ge, Y. Chen, M. Cao and Y. Qin, *Nano Res.*, 2017, **10**, 1595–1607.

48 M. Zhang, C. Han, W. Q. Cao, M. S. Cao, H. J. Yang and J. Yuan, *Nano-Micro Lett.*, 2021, **13**, 27.

49 Z. Zhang, J. Tan, W. Gu, H. Zhao, J. Zheng, B. Zhang and G. Ji, *Chem. Eng. J.*, 2020, **395**, 125190.

50 M. S. Cao, X. X. Wang, M. Zhang, J. C. Shu, W. Q. Cao, H. J. Yang, X. Y. Fang and J. Yuan, *Adv. Funct. Mater.*, 2019, **29**, 1807398.

51 W. Gu, X. Cui, J. Zheng, J. Yu, Y. Zhao and G. Ji, *J. Mater. Sci. Technol.*, 2021, **67**, 265–272.

52 M. S. Cao, X. X. Wang, M. Zhang, W. Q. Cao, X. Y. Fang and J. Yuan, *Adv. Mater.*, 2020, **32**, 1907156.

53 W. Jang, S. Mallesh, S. B. Lee and K. H. Kim, *Curr. Appl. Phys.*, 2020, **20**, 525–530.

54 J. Fang, Y. Shang, Z. Chen, W. Wei, Y. Hu, X. Yue and Z. Jiang, *J. Mater. Chem. C*, 2017, **5**, 4695–4705.

55 M. Cao, X. Wang, W. Cao, X. Fang, B. Wen and J. Yuan, *Small*, 2018, **14**, 1800987.

56 B. Quan, W. Gu, J. Sheng, X. Lv, Y. Mao, L. Liu, X. Huang, Z. Tian and G. Ji, *Nano Res.*, 2021, **14**, 1495–1501.